Aeroacoustic Analysis of a Subsonic Jet using the Discontinuous Galerkin Method

Daniel Lindblad*, Spencer Sherwin† and Chris Cantwell ‡
Imperial College London, London, SW7 2AZ, United Kingdom

Jack Lawrence§
University of Southampton, Southampton, SO17 1BJ, United Kingdom

Anderson Proença¶
Cranfield University, Cranfield, MK43 0AL, United Kingdom

Margarida Moragues Ginard‖
Basque Center for Applied Mathematics, Bilbao, 48009, Spain

In this work, the open-source spectral/hp element framework Nektar++ (www.nektar.info) is coupled with the Antares library (www.cerfacs.fr/antares/) to predict noise from a subsonic jet. Nektar++ uses the high-order discontinuous Galerkin method to solve the compressible Navier-Stokes equations on unstructured grids. Unresolved turbulent scales are modeled using an implicit Large Eddy Simulation approach. In this approach, the favourable dissipation properties of the discontinuous Galerkin method are used to remove the highest resolved wavenumbers from the solution. For time-integration, an implicit, matrix-free, Newton-Krylov method is used. To compute the far-field noise, Antares solves the Ffowcs Williams - Hawkings equation for a permeable integration surface in the time-domain using a source-time dominant algorithm. The simulation results are validated against experimental data obtained in the Doak Laboratory Flight Jet Rig, located at the University of Southampton.

I. Nomenclature

Roman/Greek

c	=	speed of sound, m s^{-1}
D_j	=	diameter of nozzle, m
E	=	total energy, kg m^{-1} s^{-2}
f	=	frequency, s^{-1}
f_i^c	=	convective flux in i^{th} spatial direction
f_i^v	=	diffusive flux in i^{th} spatial direction
M_a	=	acoustic Mach number
n_i	=	Cartesian surface normal component
p	=	pressure, kg m^{-1} s^{-2}
P	=	polynomial degree
q	=	vector of conservative variables
r	=	distance between microphone and nozzle exit, m
t	=	time, s
T	=	temperature, K
u_i	=	Cartesian velocity component, m s^{-1}

---

*Research Associate, Department of Aeronautics, South Kensington Campus, London SW7 2AZ.

†Professor, Department of Aeronautics, South Kensington Campus, London SW7 2AZ.

‡Senior Lecturer, Department of Aeronautics, South Kensington Campus, London SW7 2AZ.

§Senior Research Fellow, Institute of Sound and Vibration Research, Highfield, Southampton SO17 1BJ, Member AIAA.

¶Research Fellow in Experimental Aerodynamics, School of Aerospace, Transport and Manufacturing, Cranfield, MK43 0AL, Member AIAA.

‖Marie Skłodowska-Curie Action-IF Researcher, Computational Mathematics, Alameda de Mazarredo 14, 48009 Bilbao.

U_j	=	velocity at nozzle exit, m s^{-1}
ΔV	=	volume of grid element, m^3
x_i	=	Cartesian coordinate, m
γ	=	ratio of specific heats
μ	=	dynamic viscosity, kg m^{-1} s^{-1}
ρ	=	density, kg m^{-3}
σ	=	damping coefficient used in sponge zone, s^{-1}
τ	=	sampling interval, s
ω	=	angular frequency, rad s^{-1}
Ω	=	computational domain

Subscripts/Superscripts

$\square_\infty$	=	far-field value
$\square^*$	=	non-dimensional quantity
$\bar{\square}$	=	time-averaged quantity
$\hat{\square}$	=	Fourier transform

II. Introduction

$\mathbf{J}$ET noise is one of the dominant sources of aircraft noise during take-off [1]. Further reductions in jet noise are therefore needed to meet the ambitious noise reduction goals set forward by the EU [2], and thereby minimize the negative impacts of commercial aviation.

High-fidelity simulations are an important tool in the development of quieter aeroengines. Unfortunately, Direct Numerical Simulations (DNS) of turbulent jets operating at realistic Reynolds numbers will remain prohibitively expensive within the foreseeable future [3]. Instead, the Large Eddy Simulation (LES) technique, in which the largest turbulent scales are resolved, and the remaining scales are modeled, is commonly used to study jet noise [3–5]. Most studies of jet noise to date have used a finite volume or a finite difference method to discretize the governing equations in space, see e.g. [6–16] and [17–22]. In some of these studies, a subgrid-scale model is used to account for the unresolved turbulent scales [7, 9–12, 14–16]. The remaining studies use a filter and/or the dissipation introduced by the spatial discretization for the same purpose [6, 8, 13, 17–22]. The grid topology also differs between different studies. In [9, 10, 13–16, 21], different types of unstructured or hybrid structured-unstructured grids are used, whereas in [6–8, 11, 12, 17–20, 22], structured grids are used. In general, unstructured grids are geometrically more versatile than structured grids. However, when a finite volume or a finite difference method is used, it is typically easier to formulate a high-order discretization on a structured grid.

In recent years, other discretization methods that are capable of reaching a high-order of accuracy on unstructured grids have been developed. These include, but are not limited to, the discontinuous Galerkin (DG) method [23, 24], the flux reconstruction (FR) method [25], the spectral-difference (SD) method [26–29], and the continuous Galerkin (CG) method [30]. Apart from the CG method, the aforementioned discretizations use a Riemann solver to couple the solution in adjacent elements. This makes it possible to introduce some level of numerical dissipation through the spatial discretization [31–35]. In recent years, several studies have explored the possibility of using this dissipation in favour of a subgrid-scale model to perform implicit LES (iLES) [36–39]. However, only a few studies to date have used the DG method to study jet noise, see e.g. [40].

The purpose of this paper is to further explore the capabilities of the DG method in the context of jet aeroacoustics. To this end, results obtained with the compressible flow solver implemented in the Nektar++ spectral/hp element framework [41–44] are compared against experimental data obtained at the Doak Laboratory Flight Jet Rig (FJR) [45], located at the University of Southampton. The FJR is designed to incorporate the effects of a flight stream. For the purpose of this work, however, only the case without a flight stream will be considered. For this case, the jet operates at an acoustic Mach number of $M_a = U_j/c_\infty = 0.6$ and a Reynolds number of $Re_j = \rho_\infty U_j D_j/\mu_\infty = 5.5 \cdot 10^5$. Since the jet is not preheated, the temperature ratio is further equal to $T_j/T_\infty = 0.9335$.

III. Numerical Setup

In this section we describe the numerical setup for computing the far-field noise. The computation is split up into two parts. In the first part, the turbulent jet is simulated using the compressible flow solver in Nektar++. The solution obtained with Nektar++ is then exported to Antares, which uses the Ffowcs Williams - Hawkings method to compute the far-field noise.

A. Flow Solver

The compressible flow solver in Nektar++ [41–44] solves the compressible Navier-Stokes equations in coupled, conservative form

$$\frac{\partial \boldsymbol{q}}{\partial t} + \frac{\partial}{\partial x_i} \left(\boldsymbol{f}_i^c(\boldsymbol{q}) - \boldsymbol{f}_i^v(\boldsymbol{q}, \nabla \boldsymbol{q}) \right) = 0. \tag{1}$$

Here, $\boldsymbol{q} = (\rho, \rho u_1, \rho u_2, \rho u_3, E)^T$ is the vector of conservative variables, $\boldsymbol{f}_i^c$ is the convective flux in the ith spatial direction, and $\boldsymbol{f}_i^v$ is the diffusive flux in the ith spatial direction. In this work, we assume that the gas is calorically perfect and obeys the ideal gas law. We also assume that the viscosity is constant and equal to the far-field value.

1. Spatial Discretization

Equation (1) is discretized in space using the discontinuous Galerkin (DG) method. In the DG method, we partition the computational domain (Ω) into N_e non-overlapping elements (Ω_e). Within each element, we then seek approximate solutions, $\boldsymbol{q}^\delta$, belonging to the finite-element space

$$\mathcal{V}^P = \left\{ \phi \in L^2(\Omega) \,\middle|\, \phi|_{\Omega_e} \in \mathcal{P}_P(\Omega_e) \right\}, \tag{2}$$

where $\mathcal{P}_P(\Omega_e)$ is the space of polynomials up to order P on Ω_e. By substituting $\boldsymbol{q}^\delta \in \mathcal{V}^P$ into Eq. (1), multiplying the resulting equation by a test-vector $\boldsymbol{v} \in \mathcal{V}^P$, and then integrating by parts over Ω_e, we obtain the weak form of Eq. (1),

$$\begin{aligned}
\int_{\Omega_e} \frac{\partial \boldsymbol{q}^\delta}{\partial t} \cdot \boldsymbol{v} \, dx &+ \int_{\partial \Omega_e} \left(\boldsymbol{f}_n^c(\boldsymbol{q}^\delta) - \boldsymbol{f}_n^v(\boldsymbol{q}^\delta, \nabla \boldsymbol{q}^\delta) \right) \cdot \boldsymbol{v} \, ds \\
&- \int_{\Omega_e} \left(\boldsymbol{f}_i^c(\boldsymbol{q}^\delta) - \boldsymbol{f}_i^v(\boldsymbol{q}^\delta, \nabla \boldsymbol{q}^\delta) \right) \cdot \frac{\partial \boldsymbol{v}}{\partial x_i} \, dx = 0.
\end{aligned} \tag{3}$$

Here, $\boldsymbol{f}_n^c = \boldsymbol{f}_i^c \, n_i$ and $\boldsymbol{f}_n^v = \boldsymbol{f}_i^v \, n_i$ denote the normal convective and diffusive flux over an element boundary ($\partial \Omega_e$), respectively. In the DG method, the solution is not required to be C^0-continuous across element boundaries. Instead, the normal fluxes appearing in the boundary integral in Eq. (3) are replaced by unique numerical fluxes, that depend on the solution in the two elements sharing the boundary. In this work, we have chosen Roe's approximate Riemann solver [46] to compute $\boldsymbol{f}_n^c$ and the Interior Penalty method [47] to compute $\boldsymbol{f}_n^v$. Details on how the Riemann solver is implemented can be found in [48]. The implementation of the IP method is further described in [44].

2. Temporal Discretization

Equation (3) is integrated in time using a second-order, singly diagonally implicit Runge-Kutta method. The nonlinear system that arises from the temporal discretization is solved using the matrix-free Newton-GMRES algorithm proposed by Brown and Saad [49], see [44] for details.

3. Turbulence Modeling

In this work, we use the implicit Large Eddy Simulation (iLES) technique to account for the unresolved turbulent scales. In iLES, the numerical dissipation of the spatial discretization is used instead of a subgrid-scale model to remove the highest resolved wavenumbers from the solution. Previous work has shown that the DG discretization in combination with Roe's approximate Riemann solver is well suited for this purpose [31, 32, 36–39, 50].

4. Non-Dimensional Variables

Following [9], we non-dimensionalize the Navier-Stokes equations using the diameter of the nozzle, the density in the far-field, the speed of sound in the far-field, and the temperature in the far-field. This leads to the following non-dimensional quantities

$$\rho^* = \frac{\rho}{\rho_\infty}, \quad u_i^* = \frac{u_i}{c_\infty}, \quad p^* = \frac{p}{\rho_\infty c_\infty^2} = \frac{p}{\gamma p_\infty}, \quad T^* = \frac{T}{T_\infty}, \quad t^* = \frac{t c_\infty}{D_j}, \quad x_i^* = \frac{x_i}{D_j}. \tag{4}$$

Here, $\square^*$ denotes a non-dimensional quantity, $\square_\infty$ denotes a far-field value, $\gamma = 1.4$ is the ratio of specific heats, and D_j is the diameter of the nozzle. Since we assume that the gas is calorically perfect, obeys the ideal gas law, and has constant viscosity, the non-dimensional viscosity and thermal conductivity can be written as

$$\mu^* = \frac{M_a}{Re_j}, \quad k^* = \frac{\mu^*}{(\gamma - 1)Pr}. \tag{5}$$

Here, $Pr = 0.72$ is the Prandtl number. The acoustic Mach number and Reynolds number in Eq. (5) are further defined as

$$M_a = \frac{U_j}{c_\infty}, \quad Re_j = \frac{\rho_\infty U_j D_j}{\mu_\infty}. \tag{6}$$

The ideal gas law expressed in terms of non-dimensional quantities finally reads

$$p^* = \frac{\rho^* T^*}{\gamma}. \tag{7}$$

Nektar++ solves Eq. (1) in dimensional form. To solve the equations in non-dimensional form, we scale the mesh by D_j, select all thermodynamic quantities such that we recover the constitutive relations in non-dimensional form, and specify boundary conditions in terms of $\boldsymbol{q}^*$.

B. Far-field Noise Prediction

1. Acoustic Analogy

In this work, we use Antares [51–53] to compute the far-field noise. Antares solves the Ffowcs Williams - Hawkings equation [54] for a permeable integration surface [55] using a source-time dominant algorithm. At present, Antares provides two solution formulations, Formulation 1A by Farassat [56] and Formulation 1C by Najafi-Yazidi et al. [57]. The main difference between these two formulations is that the latter accounts for convective effects introduced by, e.g., a flight stream. Since no flight stream is considered in this work, Formulation 1A was chosen.

Similar to most numerical studies of jet noise, the volume integral is not included in the solution of the Ffowcs Williams - Hawkings equation. This simplification is justified as long as the integration surface encloses all relevant noise sources [55], and no significant entropy or vorticity waves cross the integration surface [6, 58]. In LES computations of turbulent jets, the latter condition is typically hard to satisfy at the downstream end of the integration surface [6, 58, 59]. As a result, spurious noise is generated when entropy or vorticity waves cross the integration surface. Two methods have been proposed in the literature to overcome this problem: the method of end-caps [6] and the pressure formulation [6, 58]. In this work, we have only considered the pressure formulation. Shur et al. [6] have pointed out that the pressure formulation will not provide any notable benefits for cold jets. Therefore, an open-ended integration surface was also used. In future work, the method of end-caps will be considered.

2. Acoustic Post-Processing

The acoustic post-processing is set up to match the experimental setup as closely as possible. In particular, the non-dimensional pressure signal is first computed at the same microphone locations as in the experiments, see Fig. 1. After this, the power spectral density (PSD) is computed from the non-dimensional pressure signal using the implementation of Welch's method [60] available in SciPy v1.2.1 [61]. In Welch's method, the signal is first divided into K overlapping segments. In this work, we have chosen a 50% overlap. After this, the mean is subtracted from each segment before an energy-corrected Fast Fourier Transform (FFT) is computed

$$\hat{p}_k^*(f_n^*) = \frac{\sqrt{8/3}}{N_{\text{FFT}}} \text{FFT}\left(w(t_k^*) \left(p^*(t_k^*) - \overline{p^*(t_k^*)} \right) \right). \tag{8}$$

Here, $\hat{p}_k^*(f_n^*)$ is the nth non-dimensional Fourier coefficient for the kth segment, N_{FFT} is the number of samples within each segment, FFT denotes the "standard" Fast Fourier Transform implemented in Numpy [62], $w(t^*)$ is the Hann
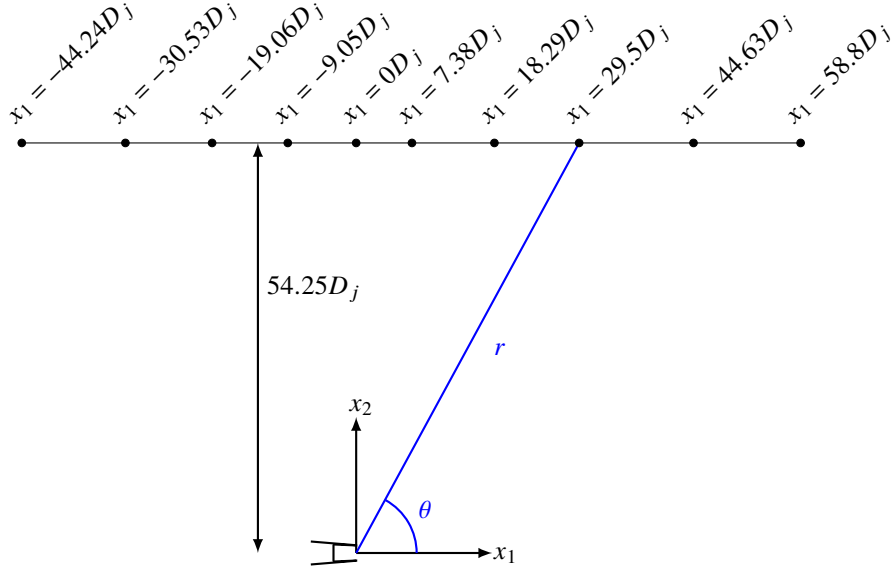
Fig. 1 Schematic view of the microphone locations.

window function, $p^*(t^*)$ is the non-dimensional pressure signal at the observer, t_k^* is a vector containing all time samples for the kth segment, and $\sqrt{8/3}$ is a factor that compensates for the energy loss introduced by the Hann window. From Eq. (8), we obtain the one-sided PSD for the kth segment as

$$\hat{P}_k^*(f_n^*) = 2\tau_{\text{FFT}}^*|\hat{p}_k^*(f_n^*)|^2, \quad f_n^* > 0. \tag{9}$$

Here, $\tau_{\text{FFT}}^* = N_{\text{FFT}}\Delta t_{\text{FW-H}}^*$ is the non-dimensional time interval covered by each segment. Finally, the PSD is obtained as the average over all segments

$$\hat{P}^*(f_n^*) = \frac{1}{K}\sum_{k=1}^{K}\hat{P}_k^*(f_n^*). \tag{10}$$

Here, K denotes the number of segments. Since the time signal recorded in the simulation will be significantly shorter than in the experiments, the PSD obtained from Eq. (10) is also averaged in the circumferential direction. To this end, 36 microphones are placed uniformly around the circumference at each axial location shown in Fig. 1.

The PSD obtained from the above procedure is non-dimensional. In order to compare with experiments, we scale the PSD using the ambient conditions measured in the experiments. More precisely, we compute the PSD in [dB/St] as

$$\text{PSD}(St) = 10\log_{10}\left(\frac{(\gamma p_\infty)^2 M_a \hat{P}^*(St M_a)}{p_{\text{ref}}^2}\right) + 20\log_{10}\left(\frac{r}{r_{\text{ref}}}\right). \tag{11}$$

Here, $St = fD_j/U_j$ is the Strouhal number, $M_a = U_j/c_\infty$ is the acoustic Mach number, and $p_{\text{ref}} = 20 \cdot 10^{-6}$ Pa is the reference pressure. To stay consistent with the post-processing procedure used for the experimental data, we also scale the PSD to $r_{\text{ref}} = 1$m distance by adding $20\log_{10}(r/r_{\text{ref}})$, where r is the distance between the microphone and the nozzle exit (in meters).

C. Computational Setup

1. Computational Domain and Boundary Conditions

An axi-symmetric, funnel-shaped, computational domain is used for the isolated nozzle considered in this work, see Fig. 2. The domain includes the nozzle geometry and extends $30D_j$ radially and $50D_j$ axially away from the nozzle
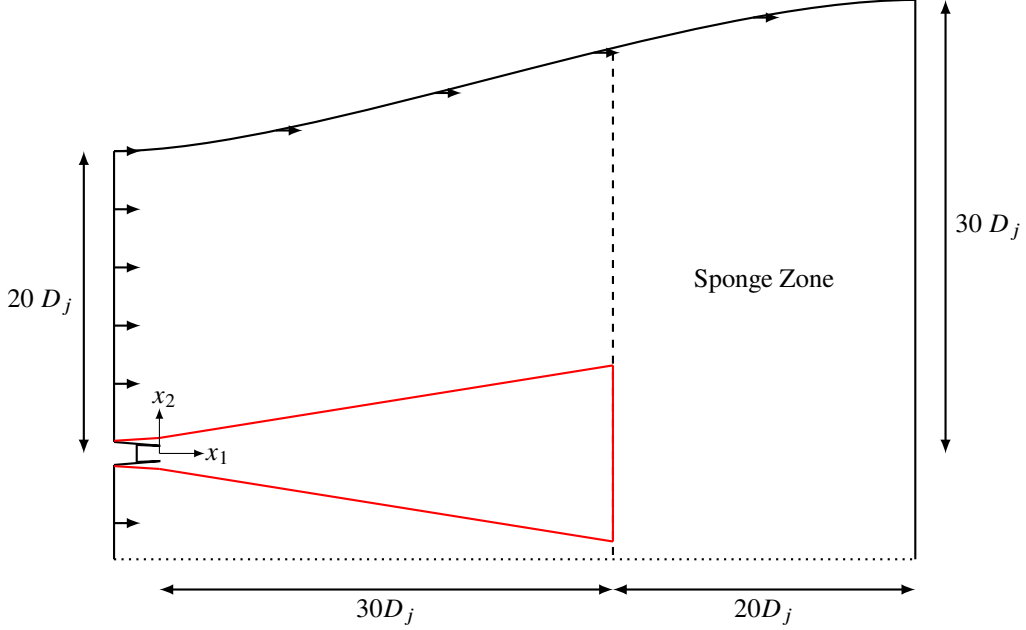
Fig. 2 Schematic view of the computational domain and Ffowcs Williams - Hawkings integration surface.

exit. The integration surface used for the Ffowcs Williams - Hawkings method extends $30D_j$ downstream. This is in line with the size recommended by Mendez et al. [59].

The inlet to the nozzle is located $1.5D_j$ upstream of the nozzle exit. At this boundary, non-uniform profiles of stagnation pressure and temperature are imposed. These profiles are selected to ensure that the mean velocity profile matches the experimental data as closely as possible at the nozzle exit. In addition to the mean velocity, several studies have demonstrated the importance of getting the turbulence levels at the nozzle exit right [14, 20]. In this work, we have not made any attempt at satisfying this condition. Instead, a relatively low resolution in combination with a no-slip boundary is used to model the flow near the wall.

Along the far-field boundaries, we add a small co-flow corresponding to 2% of the jet velocity. This is done to ensure that vortical structures generated in the jet are removed from the domain, and to facilitate flow entrainment. Finally, at the outlet, the far-field static pressure is imposed. All boundary conditions are imposed weakly through the Riemann solver [48]. This implies that the far-field boundaries, where a complete thermodynamic state is imposed, will be non-reflecting for normally incident waves if the Riemann solver correctly differentiates between incoming and outgoing waves. The Riemann solver selected in this work approximately satisfies this condition.

To prevent spurious reflections against the outlet, a sponge zone [63] is added upstream of the outlet, see Fig. 2. In this zone, the right hand side of Eq. (1) is augmented with a damping term according to

$$... = -\sigma(x_1)\left(\boldsymbol{q} - \overline{\boldsymbol{q}}\right). \tag{12}$$

Here, $\overline{\boldsymbol{q}}$ denotes a time-averaged reference solution. This solution is obtained from a separate RANS computation in STAR-CCM+ v2019.2 using the $k - \omega$ SST turbulence model. As discussed in [64], the best results are obtained when the damping coefficient $\sigma(x_1)$ is smoothly increased over a long distance. Therefore, we use the following damping coefficient

$$\sigma(x_1) = \begin{cases} 0 & x_1 < x_{s_1}, \\ \sigma_{\max} S\left(\frac{x_1 - x_{s_1}}{x_{s_2} - x_{s_1}}\right) & x_1 \in (x_{s_1}, x_{s_2}), \\ \sigma_{\max} & x_1 > x_{s_2}. \end{cases} \tag{13}$$

Here, $(x_{s_1}, x_{s_2}) = (30D_j, 50D_j)$ denotes the interval where the sponge is ramped up, $\sigma_{\max}$ is the maximum value of the damping coefficient, and $S(\xi)$ is the smooth-step function

$$S(\xi) = 6\xi^5 - 15\xi^4 + 10\xi^3 \quad \xi \in (0, 1). \tag{14}$$
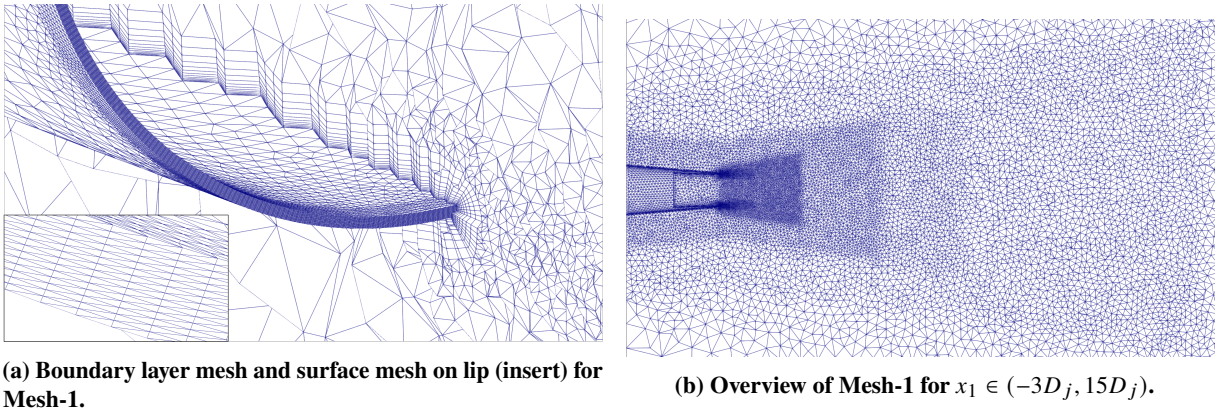
The smooth-step function is shown in Fig. 3. As can be seen from this figure, it increases smoothly from 0 to 1 over the interval $(0, 1)$.
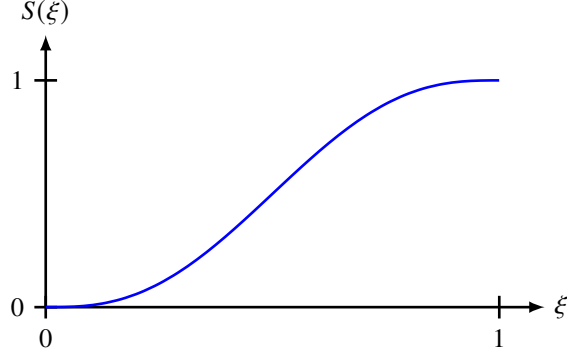
Fig. 3   Smooth-step function.

2. Computational Mesh

An unstructured mesh topology has been developed for the isolated nozzle considered in this work. The mesh is generated in a three-step procedure. In the first step, a triangular surface mesh is created using the open-source mesh generator Gmsh [65]. In the second step, a volume mesh is created from the surface mesh using STAR-CCM+ v2019.2. In particular, the *Advancing Layer Mesher* and the *Tetrahedral Mesher* in STAR-CCM+ are used to create a single prism layer around the nozzle wall, and the remaining volume mesh, respectively. Finally, in the third step, the mesh is projected onto the underlying CAD using the NekMesh [42] utility, which is part of the Nektar++ framework. In this step, the single prism layer is also split into several prism elements to improve the resolution of the boundary layer. In general, prismatic elements are useful for resolving sharp flow gradients in the wall-normal direction. At the nozzle lip, however, prismatic elements are not optimal for resolving the initial part of the shear layer. This is because the radial resolution is dictated by the size of the surface mesh on the nozzle lip. Therefore, a very large number of elements are needed on the nozzle lip to maintain sufficient resolution of the shear layer. To partly overcome this drawback, an anisotropic surface mesh is used on the nozzle lip, see Fig. 4a

(a) Boundary layer mesh and surface mesh on lip (insert) for Mesh-1.

(b) Overview of Mesh-1 for $x_1 \in (-3D_j, 15D_j)$.

**Fig. 4   Unstructured computational mesh.**

A single mesh was generated with the aforementioned procedure, see Fig. 4. As can be seen from this figure, several refinement zones were used to control the size of the tetrahedral elements in the jet plume. The boundary layer was further discretized with 13 elements in the wall normal direction, and one element per boundary layer thickness in

the streamwise and spanwise directions. It is important to point out that, although each element contains more than one degree of freedom (DOF) in the DG method, this resolution is not sufficient for wall-modeled or wall-resolved LES [66]. As a result, the present mesh is only suitable for resolving the mean velocity profile. More details about the computational mesh are provided in Table 1.

Table 1   Mesh settings.

Name	Order	N_{prism}	N_{tet}
Mesh-1	2	0.6M	4.1M

The mesh size along the lipline and the acoustic integration surface denoted "FWH-1" in Table 2 are reported in Fig. 5. The left axis in this figure gives the mesh size as the cubic root of the element volume, normalized by the diameter of the nozzle. Since each element contains more than one DOF in the DG method, we also provide an "equivalent mesh size" on the right axis in Fig. 5. This size is obtained by dividing the volume of the element by the number of degrees of freedom per element ($DOFpE$) before taking the cubic root. For the simulation reported in this paper, we have selected the polynomial degree to $P = 2$. For a tetrahedral element, $DOFpE = 10$ when $P = 2$.
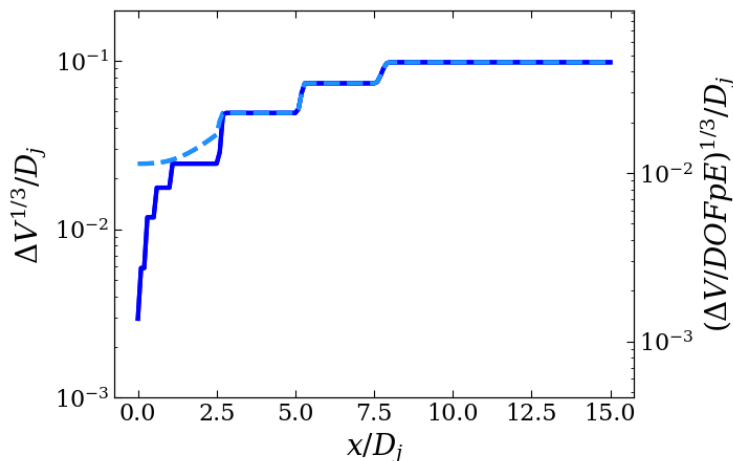
Fig. 5   Mesh size along the lipline (———) and the acoustic integration surface denoted "FWH-1" in Table 2 (- - - -).

3. Simulation Parameters

A steady RANS solution was used to initialize the LES simulation. This solution was obtained with STAR-CCM+ v2019.2 using the $k - \omega$ SST turbulence model. The LES simulation was first run for 350 non-dimensional (acoustic) time-units to remove the initial transient. After this, the simulation was continued for an additional 320 non-dimensional time-units. During this time, the conservative variables were sampled every 20th time-step at a set of linear arrays in the jet. To improve statistical convergence, 8 arrays were placed uniformly around the circumference. The conservative variables were also sampled on the two acoustic integration surfaces defined in Table 2, but at a lower frequency corresponding to every 40th time-step. The time-step used in the LES simulation was set to $\Delta t^* = 0.002$. A summary of the numerical settings is provided in Table 3.

Table 2   Specification of integration surfaces used for the Ffowcs Williams - Hawkings method.

Name	Length	$r(x_1 = 0D_j)$	$r(x_1 = 30D_j)$	Spreading Rate
FWH-1	$30D_j$	$0.75D_j$	$6.75D_j$	0.2
FWH-2	$30D_j$	$1.25D_j$	$7.25D_j$	0.2

Table 3 Numerical settings.

Name	P	DOF	$\frac{\Delta t\, c_\infty}{D_j}$	$\frac{\Delta t_{\text{jet}}\, c_\infty}{D_j}$	$\frac{\Delta t_{\text{FW–H}}\, c_\infty}{D_j}$	$\frac{\tau_{\text{init}}\, c_\infty}{D_j}$	$\frac{\tau_{\text{sample}}\, c_\infty}{D_j}$	Initialize from	Mesh
Acoustic-1	2	52M	0.002	0.04	0.08	350	320	RANS	Mesh-1

In [10], the highest resolved Strouhal number is estimated from the LES resolution at the integration surface and the number of points per wavelength required by the spatial discretization. Since the dissipation and dispersion properties of the DG method depend on both the mesh size and the polynomial order [31], we propose a generalization of the equation presented in [10] for the DG method

$$St_{\text{lim}} = \frac{D_j (DOFpE/\Delta V)^{1/3}}{M_a\, DOFpW}. \tag{15}$$

Here, ΔV denotes the volume of a grid element at the integration surface, $DOFpW$ denotes the number of degrees of freedom per wavelength required by the spatial discretization, and $DOFpE$ is the number of degrees of freedom per element. Since the grid size varies along the integration surface, ΔV in Eq. (15) is not well defined. In [14], it is suggested that ΔV is chosen to be the largest element in the range $0 < x_1/D_j < 10$. If we adopt this definition, we can use the right axis in Fig. 5 to obtain the value of the numerator in Eq. (15). We then choose $DOFpW$ based on the 1% rule suggested by Moura et al. [31]. Combined with the acoustic Mach number of the jet, these values give an estimate of $St_{\text{lim}} \approx 5$. We also note that $DOFpW$ will represent the number of points per wavelength when $DOFpE = 1$. Therefore, Eq. (15) is equivalent to the equation proposed in [10] when the finite volume or the finite difference method is used.

IV. Experimental Setup

The experimental data used in this paper were recorded in the Doak Laboratory Flight Jet Rig (FJR), located at the University of Southampton. The following sub-sections present information about the facility, instrumentation, and experimental data post-processing.

A. Facility and Hardware

The Doak Laboratory is an anechoic chamber, fully anechoic above 400 Hz with dimensions approximately equal to 15 m-long, 7 m-wide and 5 m-high. The recently commissioned Flight Jet Rig (FJR) consists of two separate air supply systems that allow in-flight simulations of single-stream, subsonic jet flows. The primary 'core' jet flow is supplied by a high-pressure compressor-reservoir system, capable of producing a maximum inlet pressure of 20 Bar. The secondary 'flight' jet flow is supplied by a 1.1 pressure ratio fan. The 300 mm-diameter flight nozzle can produce flow velocities up to Mach 0.3.

The 40 mm-diameter, round jet nozzle used in this work has a convergence half-angle of 2.5°. The total nozzle length is $19D_j$ and the nozzle contraction ratio is equal to 7. Photographs of the Doak Laboratory during the far-field, near-field, and flow-field campaigns are displayed in Fig. 6. Further information about the Doak Laboratory, the FJR, and the flight and core jet nozzles can be found in reference [45].

B. Instrumentation

A DANTEC StreamLine Pro constant temperature anemometry system was used to acquire the instantaneous velocity field and local flow temperature data. A DANTEC 55P11 miniature platinum-plated tungsten hot-wire probe, held by a DANTEC 55H22 right-angled probe support, was attached to an ISEL 3-axis traverse system, which allowed 600 mm-stroke (i.e., $15D_j$) independent movement along each of the x, y and z planes. Less exhaustive tests using DANTEC 55P61 cross-wires were also performed. A DANTEC 90P10 static temperature probe was secured near the sensors to account for local temperature variations in the flow. The hot-wire and cross-wire probes were calibrated at both the start and end of the test campaign using a DANTEC StreamLine automatic calibrator over the velocity range 1 - 300 m/s. The calibration coefficients were then extracted using a fourth-order polynomial curve fit. Finally, directional calibration was carried out for cross-wire probes to obtain information on the transverse velocity components.

To obtain far-field pressure data, ten 1/4" B&K Type 4939 microphone capsules with B&K Type 2670 Falcon preamplifiers were fixed to the end of 0.5m-long aluminium tubes and secured to a linear aluminium truss on the ceiling of the laboratory (i.e., at $\phi = 0°$) such that each microphone diaphragm was parallel to the jet axis. The microphones
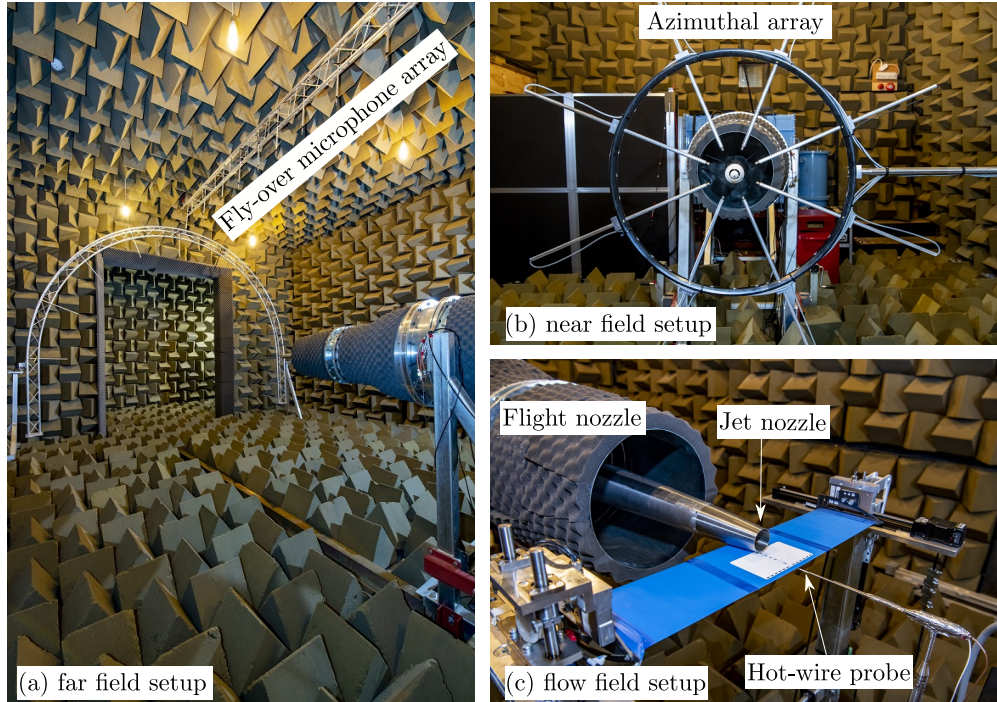
Fig. 6   Photographs of the Flight Jet Rig (FJR) in the Doak Laboratory at the University of Southampton

were positioned to record data at observer polar angles between $\theta = 40°$ and $\theta = 130°$, at $10°$ intervals. Each microphone was calibrated at both the start and end of the test campaign using a 94dB 1000kHz tone generated by a SVANTEK SV30A calibrator.

The near-field azimuthal microphone array consisted of eight 1/4" B&K Type 4939 microphone capsules with B&K Type 2670 Falcon preamplifiers fixed at the end of 0.5m-long aluminium tubes. The tubes were threaded through machined holes in aluminium blocks secured to a rigid aluminium alloy ring at $\Delta\phi = 45°$ intervals and then held in place with nylon grub screws such that each microphone pointed directly at the centre of the ring. The ring was then attached to an ISEL 2-axis traverse system and aligned with the jet axis using a nozzle laser jig.

C. Data Acquisition and Data Post-Processing

Both the hot-wire and microphone unsteady voltage data were digitised using a National Instruments PXIe-4497 Dynamic Signal Analyser at a sample rate of 200 kHz with 24-bit resolution. The hot-wire signals were acquired for 5 seconds, corrected first for temperature, using the standard method as reported by DANTEC [67], and then for velocity using the 4th-order polynomial calibration coefficients. Both the near-field and far-field microphone signals were acquired for 10 seconds, filtered using a 20 Hz high-pass filter and then amplified using B&K Type 2690 Nexus amplifiers. The time signals were corrected for amplifier gain and microphone capsule calibration sensitivity before they were transformed into the frequency domain using a Hamming window-averaged Fast Fourier Transform following Welch's overlapped segment-averaging spectral estimation method. The far-field spectra were then corrected for electronic background noise, atmospheric absorption, microphone incidence angle and distance (assuming spherical wave propagation) to yield the final free-field, 1m-lossless values. The static jet near-field spectra were only corrected for electronic background noise.

Finally, the various rig flow control transducer data were digitised using the data acquisition hardware described above. Mean values were extracted from the voltage time histories before the appropriate calibration transfer function constants were applied. The total temperatures of the flight and core jet flows were recorded directly using two National Instruments USB-TC01 devices.

V. Results

A. Validation of Coupling between Nektar++ and Antares

Nektar++ has never been coupled with the Antares library in the past. Therefore, the coupling between the two codes was validated for two generic noise sources, an acoustic monopole and an acoustic dipole. For the monopole, the comparison was done at a distance of $r = 340L$, and for the dipole, the comparison was done at a distance of $r = 30L$. Here, $L = 1$ m is the diameter of the spherical integration surface that was used to transfer information between Nektar++ and Antares.

The velocity, pressure, and density fluctuations induced by a monopole and a dipole are obtained as

$$\begin{aligned}
\boldsymbol{u}(\boldsymbol{x}, t) &= \nabla \phi(\boldsymbol{x}, t), \\
p'(\boldsymbol{x}, t) &= -\rho_\infty \frac{\partial}{\partial t} \phi(\boldsymbol{x}, t), \\
\rho'(\boldsymbol{x}, t) &= \frac{p'(\boldsymbol{x}, t)}{c_\infty^2}.
\end{aligned} \tag{16}$$

Here, $\phi(\boldsymbol{x}, t)$ is a potential function. For a monopole located at the origin, it reads

$$\phi_{\text{Monopole}}(\boldsymbol{x}, t) = \frac{A}{4\pi r} e^{i\omega\left(t - \frac{r}{c_\infty}\right)}. \tag{17}$$

Here, $r = |\boldsymbol{x}|$ is the distance from the origin and ω the angular frequency of the sound source. For a dipole aligned with the x_2-axis, the potential function reads

$$\phi_{\text{Dipole}}(\boldsymbol{x}, t) = \frac{\partial}{\partial x_2} \phi_{\text{Monopole}}(\boldsymbol{x}, t). \tag{18}$$

Analytical expressions for the monopole and the dipole have been derived in [68]. Note, however, that the dipole considered in [68] is aligned with the x_1-axis.

The comparison between Antares and the analytical solutions were performed by setting the amplitude, frequency, density, and speed of sound in Eqs. (16)-(18) to $A = 1$ m^3 s^{-1}, $\omega = 10\pi$ rad s^{-1}, $\rho_\infty = 1$ kg m^{-3}, and $c_\infty = 340$ m s^{-1}, respectively. These values have previously been used by Najafi-Yazidi et al. [57] to validate their implementation of Formulation 1C. A comparison between the analytical and numerical solutions is presented in Fig. 7. As can be seen from this figure, agreement is excellent across all observer angles for both noise sources. The results obtained for the dipole are also identical to the ones obtained by Najafi-Yazidi et al. [57] (no results for the monopole were published in [57]). This confirms that the coupling between Nektar++ and Antares works correctly.
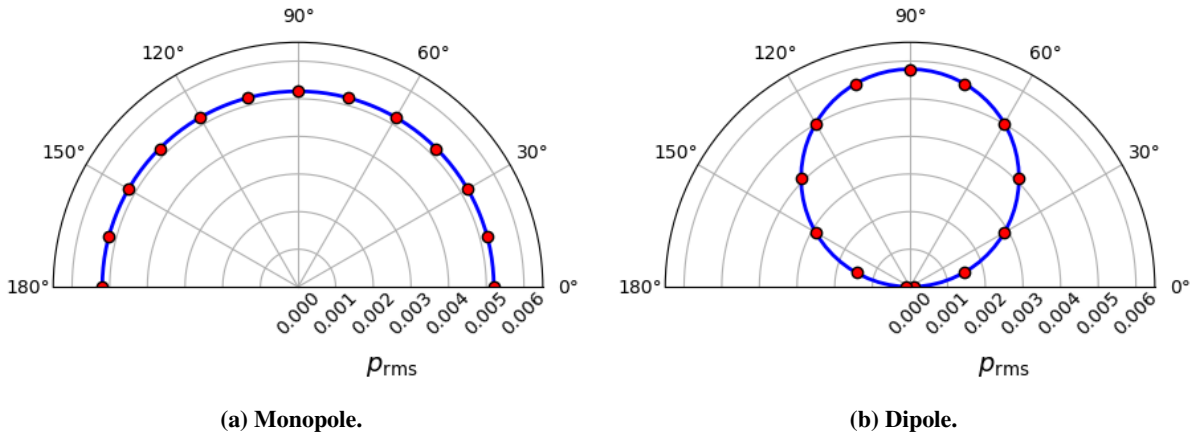

(a) Monopole. (b) Dipole.

Fig. 7 Comparison between the analytical solution (——) and the numerical solution (⬤) for two noise sources.

B. Instantaneous Flow Field

The instantaneous flow field obtained with the "Acoustic-1" simulation defined in Table 3 is illustrated by Mach number contours in Fig. 8. In this figure, the pressure field is also illustrated by normalized pressure fluctuations. The pressure field shows clear sign of acoustic waves propagating downstream. This is expected, considering that the largest sound levels are observed in the downstream direction for an isolated jet. The pressure field in Fig. 8 also indicates that sound waves are generated close to the nozzle exit. A possible source of these sound waves is the transition of the laminar boundary layer inside the nozzle into a turbulent shear layer. Indeed, the Mach number contours shown in Fig. 8 indicate that the flow is laminar inside the nozzle, and then quickly transitions into a turbulent state after the nozzle.
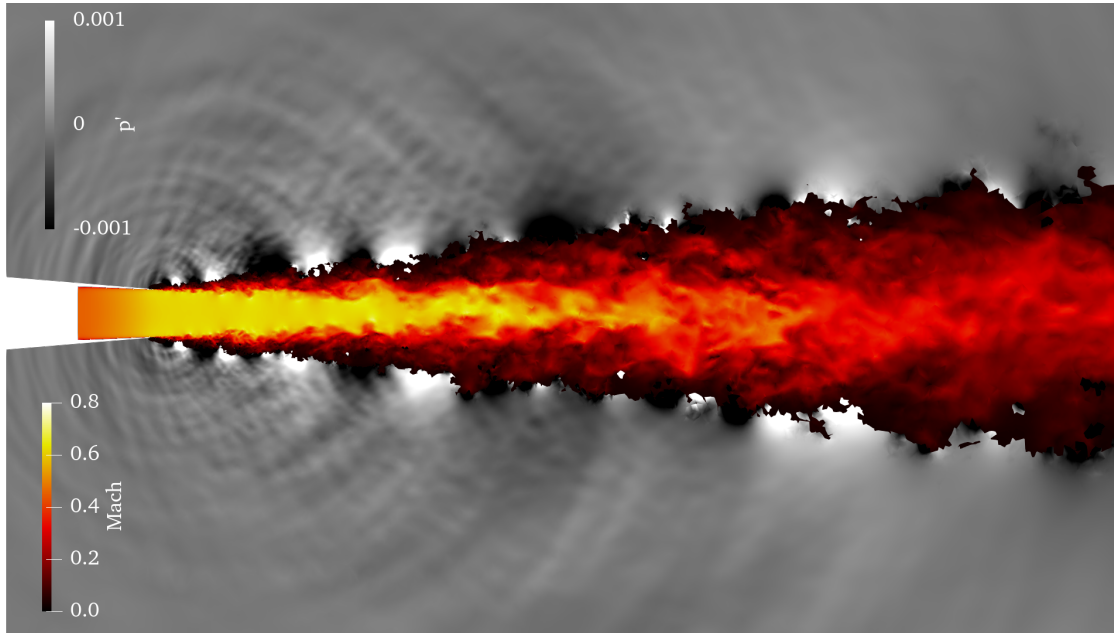
Fig. 8   Instantaneous flow field for the Acoustic-1 simulation.

C. Near-Field Flow Statistics

In this section we focus on the flow in the near-field. To begin with, we consider the mean axial velocity at the nozzle exit, shown in Fig. 9a. As can be seen from this figure, the simulation agrees quite well with the experiments. We believe that the discrepancies seen in Fig. 9a are mainly caused by the boundary layer profile imposed at the inlet to the nozzle. In particular, the boundary condition imposes a purely axial flow at this point, even though the nozzle is conical. The conical shape of the nozzle also accelerates the flow before it reaches the nozzle exit. This makes it hard to correlate the velocity profile at the nozzle exit, where experimental data is available, with the velocity profile imposed at the inlet to the computational domain.

Next, we turn our attention to the RMS of the axial velocity at the nozzle exit, shown in Fig. 9b. As can be seen from this figure, there are notable discrepancies between the simulation and the experiments. This is expected, considering that the boundary layer inside the nozzle is not properly resolved in the simulation. As shown in [14, 20], this can lead to higher noise levels in the far-field.

The evolution of the mean axial velocity downstream of the nozzle exit is shown in Fig. 10a. In general, the agreement between the simulation and the experiments is very good at all axial locations. The only notable discrepancy is found close to the centerline for $x_1 > 6D_j$. Here, the simulation over-predicts the mean axial velocity slightly. This indicates that the length of the potential core is over-predicted in the simulation. By looking at Fig. 11a, we see that this is indeed the case.

To partly explain the longer potential core found in the simulation, we can look at the turbulence levels in the jet plume shown in Fig. 10b. As can be seen from this figure, the turbulence levels are slightly under-predicted close to the centerline for $4D_j < x_1 < 6D_j$. This indicates that the simulation under-predicts turbulent mixing in this region, which in turn should lead to a longer potential core. The lower turbulence levels predicted by the simulation close to the
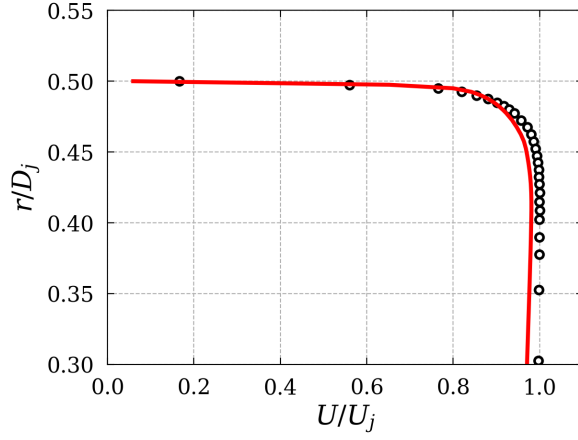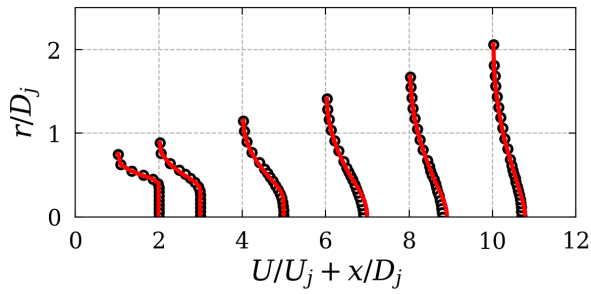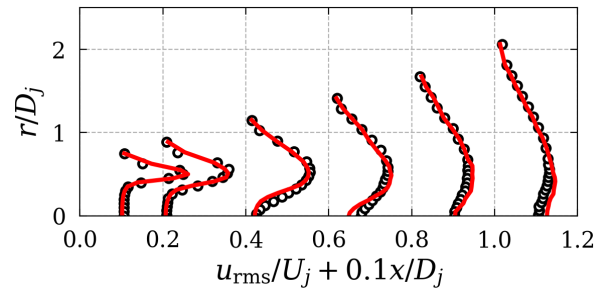
(a) Mean of axial velocity.
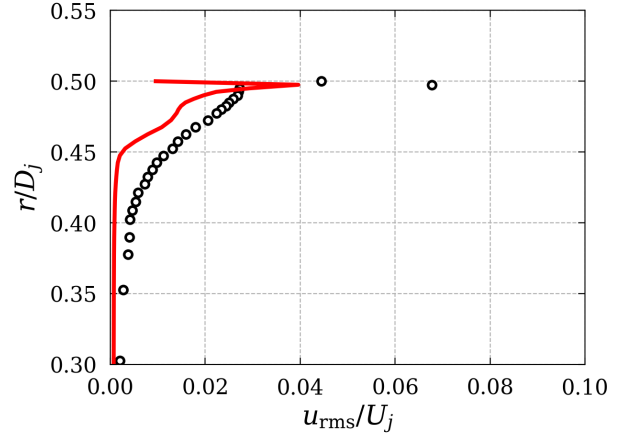
(b) RMS of axial velocity.

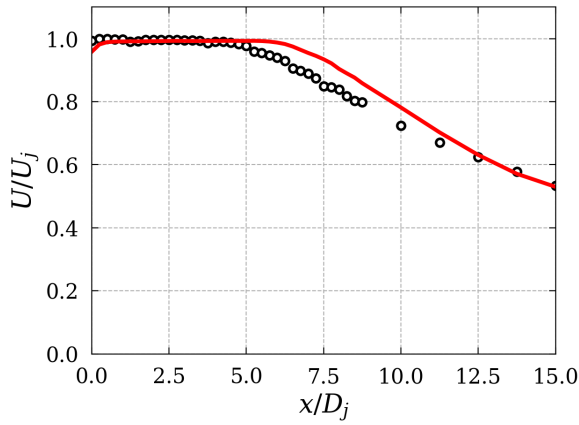**Fig. 9   Axial velocity statistics at the nozzle exit: Acoustic-1 simulation (——), experiments (○).**

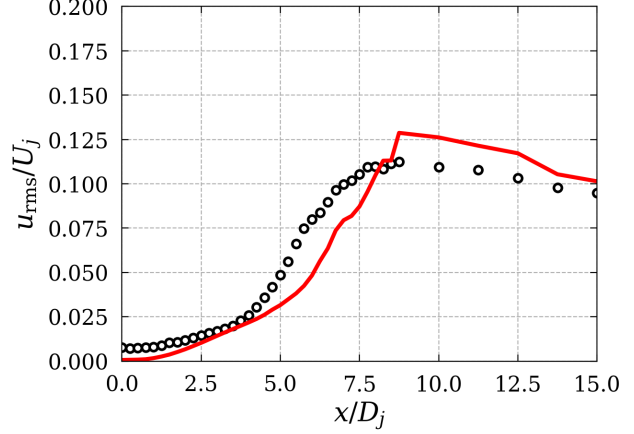

(a) Mean of axial velocity.

(b) RMS of axial velocity.

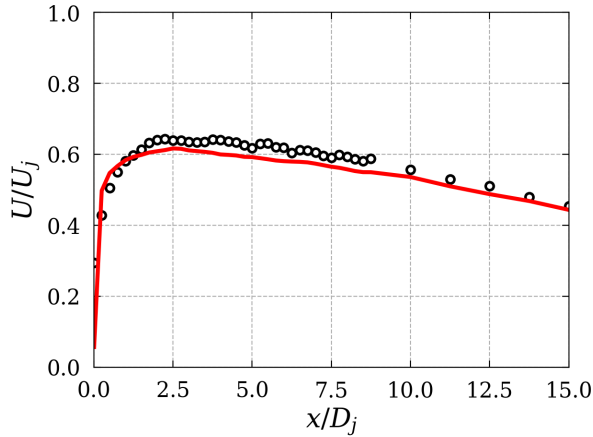**Fig. 10   Axial velocity statistics in the jet plume: Acoustic-1 simulation (——), experiments (○).**
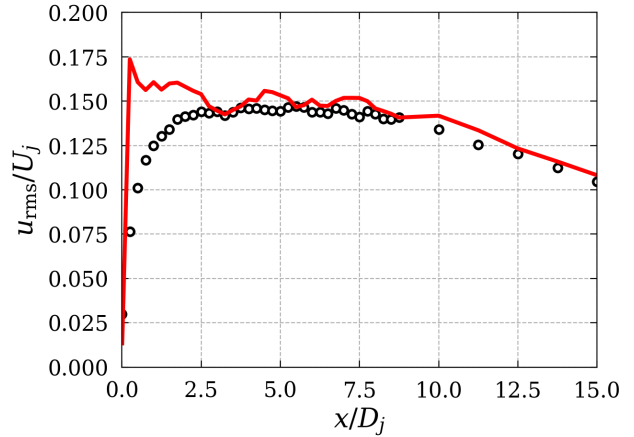
(a) Mean of axial velocity.

(b) RMS of axial velocity.

Fig. 11   Axial velocity statistics along the centerline: Acoustic-1 simulation (———), experiments (○).

(a) Mean of axial velocity.

(b) RMS of axial velocity.

Fig. 12   Axial velocity statistics along the lipline: Acoustic-1 simulation (———), experiments (○).

centerline are also clearly seen in Fig. 11b. Apart from these discrepancies, the turbulence levels in the jet plume are accurately predicted in the simulation. This is an encouraging result, especially considering that the turbulence levels were under-predicted close to the nozzle exit.

Before we move on to consider the far-field acoustics, we will consider the mean and RMS of the axial velocity along the lipline, which are shown in Fig. 12. An interesting thing that can be noted from this figure is that the RMS levels are over-predicted by the simulation close to the nozzle lip. Similar over-predictions close to the nozzle lip have been observed by Brès et al. [14] and Bogey et al. [20] when the turbulence levels at the nozzle exit were too low, and are associated with laminar to turbulence transition. In [14, 20], it was also found that simulations which over-predicted the RMS levels close to the lipline produced larger noise levels in the far-field. As will be shown next, the same holds for the simulation considered in this work.

D. Far-Field Acoustics

As explained in section III.B.1, the pressure signal is computed at the microphone locations shown in Fig. 1 using Antares. The PSD is then computed from the pressure signal using Welch's method [60], see section III.B.2 for details. The number of time samples included in each segment was chosen to be $N_{\text{FFT}} = 417$. This leads to a bin-size of $\Delta St = D_j/(N_{\text{FFT}}\Delta t_{\text{FW-H}}U_j) = 0.05$. The Nyquist Strouhal number is further equal to $St_{\text{Nyq}} = D_j/(2\Delta t_{\text{FW-H}}U_j) = 10.42$.

14

This is roughly twice as large as the highest resolved Strouhal number estimated from Eq. (15).

We begin by comparing the pressure formulation proposed in [6, 58] to the original "density formulation". To this end, we computed the far-field noise using both formulations, using both a closed and an open version of the integration surface denoted FWH-1 in Table 2. The resulting PSDs at 4 representative microphone locations are shown in Fig. 13. From this figure, two things are immediately apparent. First, we see that the pressure formulation gives identical results to the "density formulation" when a closed integration surface is used. This result is expected, considering that the pressure formulation was originally developed for hot jets [6, 58]. In [59], it was also found that the pressure formulation gives very similar results to the "density formulation" for an isothermal jet when a closed integration surface was used. The second thing that can be noted from Fig. 13 is that the closed surface leads to significantly higher noise levels for lower frequencies. As a result, the open surface gives much better agreement with experiments.

(a) $\theta = 43°$

(b) $\theta = 61°$

(c) $\theta = 90°$

(d) $\theta = 109°$
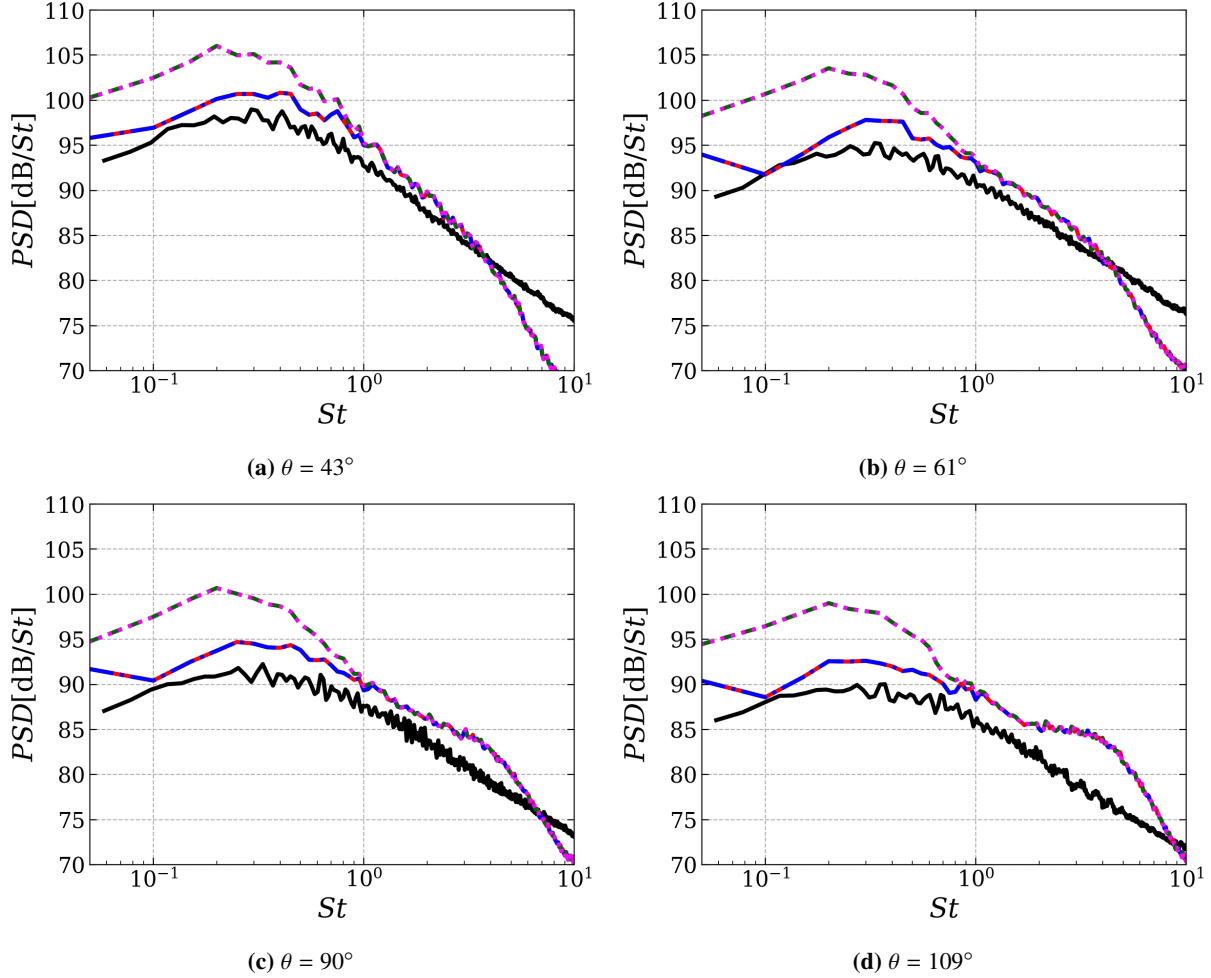
Fig. 13   Power spectral density in the far-field obtained with the Acoustic-1 simulation and the (narrow) FWH-1 integration surface, using the "density formulation" + open end-cap (——), the pressure formulation [6, 58] + open end-cap (–·–·–), the "density formulation" + closed end-cap (– – –) and the pressure formulation [6, 58] + closed end-cap (······). Experimental data is represented by solid black lines (——).

Next, we compare results obtained with the two integration surfaces defined in Table 2. Since the pressure formulation gives no advantage in our case, the comparison was done using the original "density formulation". To avoid contaminating the noise signal, we also do the comparison without an end-cap. The results obtained with the two integration surfaces are shown in Fig. 14. As can be seen from this figure, the two surfaces give virtually identical results. This indicates that the narrow surface (denoted FWH-1 in Table 2) is already wide enough to enclose all relevant noise sources.

(a) $\theta = 43°$

(b) $\theta = 61°$

(c) $\theta = 90°$

(d) $\theta = 109°$
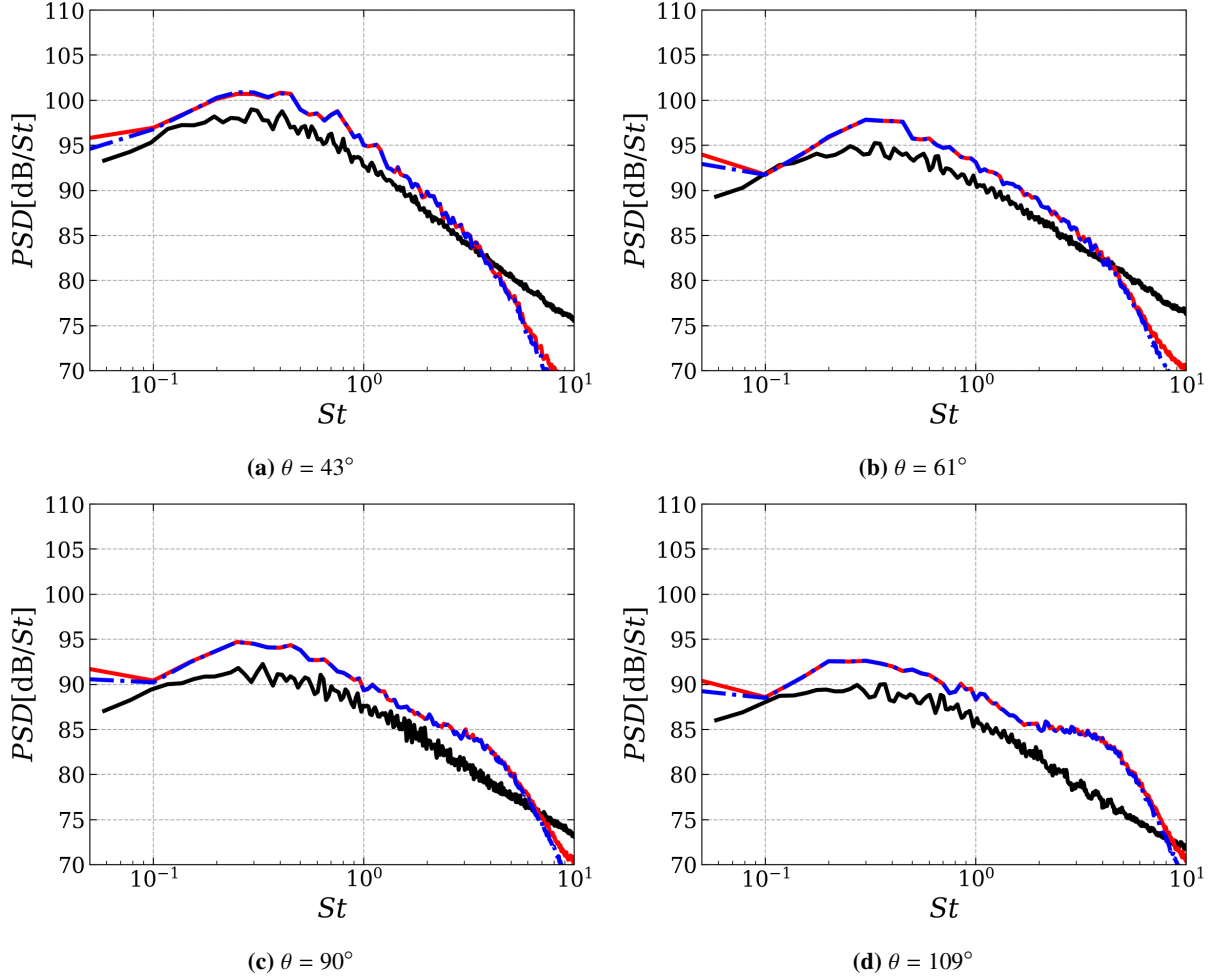
Fig. 14   Power spectral density in the far-field obtained with the Acoustic-1 simulation and the "density formulation", using the (narrow) FWH-1 integration surface (⎯⎯) and the (wide) FWH-2 integration surface (⋅⋅⋅⋅⋅). Experimental data is represented by solid black lines (⎯⎯).

The results shown in Fig. 14 also indicate that the present LES over-predicts the experiments by approximately 2.5dB across all observer angles. One possible explanation for this discrepancy is the laminar boundary layer inside the nozzle, and the associated transition into a turbulent shear layer pointed out earlier. However, it is not possible to say at this point how much this factor influences the acoustic results.

Apart from the relatively constant offset in the far-field noise, the present LES accurately predicts the shape of the spectra, including the peak frequency. Based on the relatively smooth shape of the PSD for lower frequencies, we can also say that the spectra is relatively well converged. Finally, based on the shape of the spectra shown in Fig. 14, we find that the highest resolved Strouhal number is around $St_{\mathrm{lim}} \approx 4$. This is quite close to $St_{\mathrm{lim}} \approx 5$ estimated from Eq. (15).

VI. Conclusions

The noise produced by an isolated jet operating at an acoustic Mach number of $M_a = 0.6$ and a Reynolds number of $Re = 5.5 \cdot 10^5$ was computed by coupling the compressible flow solver in the spectral/hp element framework Nektar++ [41–44] with the Ffowcs Williams - Hawkings method in the Antares library [51–53]. The compressible flow solver in Nektar++ uses the high-order discontinuous Galerkin (DG) method to discretize the compressible Navier-Stokes equations on unstructured grids. In this work, we selected the polynomial degree in the DG method to $P = 2$, which gives a third-order accurate discretization in space. For time integration, we used a second-order accurate singly diagonally implicit Runge-Kutta method. To account for the unresolved turbulent scales, an implicit Large Eddy Simulation

approach was used.

The simulation results were validated against experimental data obtained at the Doak Laboratory Flight Jet Rig [45], located at the University of Southampton. In general, the near-field flow statistics obtained from the simulation were found to agree well with those obtained from experiments. The largest discrepancies were found close to the nozzle exit. In particular, the turbulence levels at the nozzle exit were under predicted in the simulation. This is expected since the turbulent boundary layer inside the nozzle was not properly resolved in the simulation. As a result, the shear layer transitions into a turbulent state close the the nozzle exit. This does in turn lead to an over-prediction of the RMS of the axial velocity in the initial part of the shear layer.

In terms of far-field acoustics, it is found that the simulation correctly predicts the shape of the spectra up to the highest resolved Strouhal number, which is around $St_{\mathrm{lim}} \approx 4$ in this work. However, the noise levels predicted by the simulation are approximately 2.5dB larger than in the experiments. Previous research has shown that a laminar boundary layer can lead to additional noise in the far-field, see e.g. [14, 20] and the references cited therein. It is therefore reasonable to assume that the laminar boundary layer observed in this work is one of the reasons the simulation predicts higher noise levels in the far-field. However, more work is needed to determine the relative importance of this error source.

References

[1] Envia, E., "Noise emissions from commercial aircraft," *Green Aviation: Reduction of Environmental Impact Through Aircraft Technology and Alternative Fuels*, edited by E. S. Nelson and D. R. Reddy, CRC Press, Leiden, The Netherlands, 2017, 1st ed. https://doi.org/10.1201/b20287.

[2] European Commission, *Flightpath 2050, Europe's Vision for Aviation*, European Union, 2011. https://doi.org/10.2777/50266.

[3] Lyrintzis, A. S., and Coderoni, M., "Overview of the Use of Large-Eddy Simulations in Jet Aeroacoustics," *AIAA Journal*, Vol. 58, No. 4, 2020, pp. 1620–1638. https://doi.org/10.2514/1.J058498.

[4] Bodony, D. J., and Lele, S. K., "Current Status of Jet Noise Predictions Using Large-Eddy Simulation," *AIAA Journal*, Vol. 46, No. 2, 2008, pp. 364–380. https://doi.org/10.2514/1.24475.

[5] Brès, G. A., and Lele, S. K., "Modelling of jet noise: a perspective from large-eddy simulations," *Philosophical Transactions of the Royal Society A: Mathematical, Physical and Engineering Sciences*, Vol. 377, No. 2159, 2019, p. 20190081. https://doi.org/10.1098/rsta.2019.0081.

[6] Shur, M. L., Spalart, P. R., and Strelets, M. K., "Noise Prediction for Increasingly Complex Jets. Part I: Methods and Tests," *International Journal of Aeroacoustics*, Vol. 4, No. 3, 2005, pp. 213–245. https://doi.org/10.1260/1475472054771376.

[7] Andersson, N., Eriksson, L.-E., and Davidson, L., "Large-Eddy Simulation of Subsonic Turbulent Jets and Their Radiated Sound," *AIAA Journal*, Vol. 43, No. 9, 2005, pp. 1899–1912. https://doi.org/10.2514/1.13278.

[8] Shur, M. L., Spalart, P. R., and Strelets, M. K., "LES-based evaluation of a microjet noise reduction concept in static and flight conditions," *Journal of Sound and Vibration*, Vol. 330, No. 17, 2011, pp. 4083–4097. https://doi.org/10.1016/j.jsv.2011.02.013.

[9] Brès, G., Nichols, J., Lele, S., and Ham, F., "Towards Best Practices for Jet Noise Predictions with Unstructured Large Eddy Simulations," *42nd AIAA Fluid Dynamics Conference and Exhibit*, New Orleans, LA, 2012. https://doi.org/10.2514/6.2012-2965.

[10] Mendez, S., Shoeybi, M., Sharma, A., Ham, F. E., Lele, S. K., and Moin, P., "Large-Eddy Simulations of Perfectly Expanded Supersonic Jets Using an Unstructured Solver," *AIAA Journal*, Vol. 50, No. 5, 2012, pp. 1103–1118. https://doi.org/10.2514/1.J051211.

[11] Shur, M. L., Spalart, P. R., and Strelets, M. K., "Jet noise computation based on enhanced DES formulations accelerating the RANS-to-LES transition in free shear layers," *International Journal of Aeroacoustics*, Vol. 15, No. 6-7, 2016, pp. 595–613. https://doi.org/10.1177/1475472X16659388.

[12] Lorteau, M., Cléro, F., and Vuillot, F., "Analysis of noise radiation mechanisms in hot subsonic jet from a validated large eddy simulation solution," *Physics of Fluids*, Vol. 27, No. 7, 2015. https://doi.org/10.1063/1.4926792.

[13] Tyacke, J., Naqvi, I., Wang, Z.-N., Tucker, P., and Boehning, P., "Predictive Large Eddy Simulation for Jet Aeroacoustics–Current Approach and Industrial Application," *Journal of Turbomachinery*, Vol. 139, No. 8, 2017. https://doi.org/10.1115/1.4035662.

[14] Brès, G. A., Jordan, P., Jaunet, V., Le Rallic, M., Cavalieri, A. V. G., Towne, A., Lele, S. K., Colonius, T., and Schmidt, O. T., "Importance of the nozzle-exit boundary-layer state in subsonic turbulent jets," *Journal of Fluid Mechanics*, Vol. 851, 2018, p. 83–124. https://doi.org/10.1017/jfm.2018.476.

[15] Tyacke, J. C., Wang, Z.-N., and Tucker, P. G., "LES–RANS of Installed Ultra-High-Bypass-Ratio Coaxial Jet Aeroacoustics with Flight Stream," *AIAA Journal*, Vol. 57, No. 3, 2019, pp. 1215–1236. https://doi.org/10.2514/1.J057057.

[16] Wang, Z.-N., Proenca, A., Lawrence, J., Tucker, P. G., and Self, R., "Large-Eddy-Simulation Prediction of an Installed Jet Flow and Noise with Experimental Validation," *AIAA Journal*, Vol. 58, No. 6, 2020, pp. 2494–2503. https://doi.org/10.2514/1.J058921.

[17] Uzun, A., and Hussaini, M. Y., "Simulation of Noise Generation in the Near-Nozzle Region of a Chevron Nozzle Jet," *AIAA Journal*, Vol. 47, No. 8, 2009, pp. 1793–1810. https://doi.org/10.2514/1.36659.

[18] Uzun, A., Bin, J., and Hussaini, M. Y., "High-Fidelity Numerical Simulation of a Chevron Nozzle Jet Flow," *International Journal of Aeroacoustics*, Vol. 10, No. 5-6, 2011, pp. 531–564. https://doi.org/10.1260/1475-472X.10.5-6.531.

[19] Bogey, C., Marsden, O., and Bailly, C., "Large-eddy simulation of the flow and acoustic fields of a Reynolds number 10^5 subsonic jet with tripped exit boundary layers," *Physics of Fluids*, Vol. 23, No. 3, 2011, pp. 035104–1–035104–20. https://doi.org/10.1063/1.3555634.

[20] Bogey, C., Marsden, O., and Bailly, C., "Influence of initial turbulence level on the flow and sound fields of a subsonic jet at a diameter-based Reynolds number of 10^5," *Journal of Fluid Mechanics*, Vol. 701, 2012, p. 352–385. https://doi.org/10.1017/jfm.2012.162.

[21] Faranosov, G. A., Goloviznin, V. M., Karabasov, S. A., Kondakov, V. G., Kopiev, V. F., and Zaitsev, M. A., "CABARET method on unstructured hexahedral grids for jet noise computation," *Computers and Fluids*, Vol. 88, 2013, pp. 165–179. https://doi.org/10.1016/j.compfluid.2013.08.011.

[22] Bogey, C., and Marsden, O., "Simulations of Initially Highly Disturbed Jets with Experiment-Like Exit Boundary Layers," *AIAA Journal*, Vol. 54, No. 4, 2016, pp. 1299–1312. https://doi.org/10.2514/1.J054426.

[23] Reed, W. H., and Hill, T., "Triangular mesh methods for the neutron transport equation," Technical Report LA-UR-73-479, Los Alamos Scientific Laboratory, 1973.

[24] Cockburn, B., Karniadakis, G. E., and Shu, C.-W., "The Development of Discontinuous Galerkin Methods," *Discontinuous Galerkin Methods*, Springer Berlin Heidelberg, 2000, pp. 3–50. https://doi.org/10.1007/978-3-642-59721-3_1.

[25] Huynh, H. T., "A Flux Reconstruction Approach to High-Order Schemes Including Discontinuous Galerkin Methods," *18th AIAA Computational Fluid Dynamics Conference*, Miami, FL, 2007. https://doi.org/10.2514/6.2007-4079.

[26] Kopriva, D. A., and Kolias, J. H., "A Conservative Staggered-Grid Chebyshev Multidomain Method for Compressible Flows," *Journal of Computational Physics*, Vol. 125, No. 1, 1996, pp. 244–261. https://doi.org/10.1006/jcph.1996.0091.

[27] Kopriva, D. A., "A Conservative Staggered-Grid Chebyshev Multidomain Method for Compressible Flows. II. A Semi-Structured Method," *Journal of Computational Physics*, Vol. 128, No. 2, 1996, pp. 475–488. https://doi.org/10.1006/jcph.1996.0225.

[28] Kopriva, D. A., "A Staggered-Grid Multidomain Spectral Method for the Compressible Navier–Stokes Equations," *Journal of Computational Physics*, Vol. 143, No. 1, 1998, pp. 125–158. https://doi.org/10.1006/jcph.1998.5956.

[29] Liu, Y., Vinokur, M., and Wang, Z., "Spectral difference method for unstructured grids I: Basic formulation," *Journal of Computational Physics*, Vol. 216, No. 2, 2006, pp. 780–801. https://doi.org/10.1016/j.jcp.2006.01.024.

[30] Karniadakis, G., and Sherwin, S., *Spectral/hp Element Methods for Computational Fluid Dynamics*, 2nd ed., Oxford University Press, 2005. https://doi.org/10.1093/acprof:oso/9780198528692.001.0001.

[31] Moura, R., Sherwin, S., and Peiró, J., "Linear dispersion–diffusion analysis and its application to under-resolved turbulence simulations using discontinuous Galerkin spectral/hp methods," *Journal of Computational Physics*, Vol. 298, 2015, pp. 695–710. https://doi.org/10.1016/j.jcp.2015.06.020.

[32] Mengaldo, G., Moura, R., Giralda, B., Peiró, J., and Sherwin, S., "Spatial eigensolution analysis of discontinuous Galerkin schemes with practical insights for under-resolved computations and implicit LES," *Computers and Fluids*, Vol. 169, 2018, pp. 349–364. https://doi.org/10.1016/j.compfluid.2017.09.016.

[33] Alhawwary, M., and Wang, Z., "Fourier analysis and evaluation of DG, FD and compact difference methods for conservation laws," *Journal of Computational Physics*, Vol. 373, 2018, pp. 835–862. https://doi.org/10.1016/j.jcp.2018.07.018.

[34] Vincent, P., Castonguay, P., and Jameson, A., "Insights from von Neumann analysis of high-order flux reconstruction schemes," *Journal of Computational Physics*, Vol. 230, No. 22, 2011, pp. 8134–8154. https://doi.org/10.1016/j.jcp.2011.07.013.

[35] Vermeire, B., and Vincent, P., "On the properties of energy stable flux reconstruction schemes for implicit large eddy simulation," *Journal of Computational Physics*, Vol. 327, 2016, pp. 368–388. https://doi.org/10.1016/j.jcp.2016.09.034.

[36] Uranga, A., Persson, P.-O., Drela, M., and Peraire, J., "Implicit Large Eddy Simulation of transition to turbulence at low Reynolds numbers using a Discontinuous Galerkin method," *International Journal for Numerical Methods in Engineering*, Vol. 87, No. 1-5, 2011, pp. 232–261. https://doi.org/10.1002/nme.3036.

[37] Beck, A. D., Bolemann, T., Flad, D., Frank, H., Gassner, G. J., Hindenlang, F., and Munz, C.-D., "High-order discontinuous Galerkin spectral element methods for transitional and turbulent flow simulations," *International Journal for Numerical Methods in Fluids*, Vol. 76, No. 8, 2014, pp. 522–548. https://doi.org/10.1002/fld.3943.

[38] Carton de Wiart, C., Hillewaert, K., Bricteux, L., and Winckelmans, G., "Implicit LES of free and wall-bounded turbulent flows based on the discontinuous Galerkin/symmetric interior penalty method," *International Journal for Numerical Methods in Fluids*, Vol. 78, No. 6, 2015, pp. 335–354. https://doi.org/10.1002/fld.4021.

[39] Bergmann, M., Morsbach, C., and Franke, M., *Implicit LES of a Turbulent Channel Flow with High-Order Discontinuous Galerkin and Finite Volume Discretization*, Springer International Publishing, 2019, ERCOFTAC Series, Vol. 25, pp. 61–67. https://doi.org/10.1007/978-3-030-04915-7.

[40] Lorteau, M., de la Llave Plata, M., and Couaillier, V., "Turbulent jet simulation using high-order DG methods for aeroacoustic analysis," *International Journal of Heat and Fluid Flow*, Vol. 70, 2018, pp. 380 – 390. https://doi.org/10.1016/j.ijheatfluidflow.2018.01.012.

[41] Cantwell, C., Moxey, D., Comerford, A., Bolis, A., Rocco, G., Mengaldo, G., De Grazia, D., Yakovlev, S., Lombard, J.-E., Ekelschot, D., Jordi, B., Xu, H., Mohamied, Y., Eskilsson, C., Nelson, B., Vos, P., Biotto, C., Kirby, R., and Sherwin, S., "Nektar++: An open-source spectral/hp element framework," *Computer Physics Communications*, Vol. 192, 2015, pp. 205 – 219. https://doi.org/10.1016/j.cpc.2015.02.008.

[42] Moxey, D., Cantwell, C. D., Bao, Y., Cassinelli, A., Castiglioni, G., Chun, S., Juda, E., Kazemi, E., Lackhove, K., Marcon, J., Mengaldo, G., Serson, D., Turner, M., Xu, H., Peiró, J., Kirby, R. M., and Sherwin, S. J., "Nektar++: Enhancing the capability and application of high-fidelity spectral/hp element methods," *Computer Physics Communications*, Vol. 249, 2020. https://doi.org/10.1016/j.cpc.2019.107110.

[43] Mengaldo, G., "Discontinuous spectral/hp element methods: development, analysis and applications to compressible flows," Ph.D. thesis, Imperial College London, London, UK, 2015.

[44] Yan, Z.-G., Pan, Y., Castiglioni, G., Hillewaert, K., Peiró, J., Moxey, D., and Sherwin, S. J., "Nektar++: Design and implementation of an implicit, spectral/hp element, compressible flow solver using a Jacobian-free Newton Krylov approach," *Computers & Mathematics with Applications*, Vol. 81, 2021, pp. 351–372. https://doi.org/10.1016/j.camwa.2020.03.009.

[45] Proença, A., Lawrence, J., and Self, R., "Experimental Investigation into the Turbulence Flow Field of In-Flight Round Jets," *AIAA Journal*, Vol. 58, No. 8, 2020, pp. 1–11. https://doi.org/10.2514/1.J059035.

[46] Roe, P., "Approximate Riemann solvers, parameter vectors, and difference schemes," *Journal of Computational Physics*, Vol. 43, No. 2, 1981, pp. 357–372. https://doi.org/10.1016/0021-9991(81)90128-5.

[47] Hartmann, R., and Houston, P., "Symmetric Interior Penalty DG Methods for the Compressible Navier-Stokes Equations I: Method Formulation," *International Journal of Numerical Analysis and Modeling*, Vol. 3, No. 1, 2006, pp. 1–20.

[48] Mengaldo, G., Grazia, D. D., Witherden, F., Farrington, A., Vincent, P., Sherwin, S., and Peiro, J., "A Guide to the Implementation of Boundary Conditions in Compact High-Order Methods for Compressible Aerodynamics," *7th AIAA Theoretical Fluid Mechanics Conference*, Atlanta, GA, 2014. https://doi.org/10.2514/6.2014-2923.

[49] Brown, P. N., and Saad, Y., "Convergence Theory of Nonlinear Newton–Krylov Algorithms," *SIAM Journal on Optimization*, Vol. 4, No. 2, 1994, pp. 297–330. https://doi.org/10.1137/0804017.

[50] Moura, R., Mengaldo, G., Peiró, J., and Sherwin, S., "On the eddy-resolving capability of high-order discontinuous Galerkin approaches to implicit LES / under-resolved DNS of Euler turbulence," *Journal of Computational Physics*, Vol. 330, 2017, pp. 615–623. https://doi.org/10.1016/j.jcp.2016.10.056.

[51] antares Development Team, "Antares Documentation Release 1.17.0," , 2020. URL https://cerfacs.fr/antares/.

[52] Di Stefano, D., Rona, A., Hall, E., and Puigt, G., "Implementing the Ffowcs Williams and Hawkings acoustic analogy in Antares," *The 22nd International Congress on Sound and Vibration (ICSV22)*, Florence, Italy, 2015.

[53] Di Stefano, D., Rona, A., Hall, E., Morfey, C. L., and Puigt, G., "Validating the Ffowcs Williams and Hawkings acoustic analogy implementation in Antares," *22nd AIAA/CEAS Aeroacoustics Conference*, Lyon, France, 2016. https://doi.org/10.2514/6.2016-3059.

[54] Ffowcs Williams, J. E., and Hawkings, D. L., "Sound Generation by Turbulence and Surfaces in Arbitrary Motion," *Philosophical Transactions of the Royal Society of London. Series A, Mathematics and Physical Sciences*, Vol. 264, No. 1151, 1969, pp. 321–342. https://doi.org/10.1098/rsta.1969.0031.

[55] di Francescantonio, P., "A New Boundary Integral Formulation for the Prediction of Sound Radiation," *Journal of Sound and Vibration*, Vol. 202, No. 4, 1997, pp. 491–509. https://doi.org/10.1006/jsvi.1996.0843.

[56] Farassat, F., "Derivation of Formulations 1 and 1A of Farassat," Technical Report NASA/TM-2007-214853, NASA, Hampton, VA, March 2007.

[57] Najafi-Yazidi, A., Brès, G. A., and Mongeau, L., "An Acoustic Analogy Formulation for Moving Sources in Uniformly Moving Media," *Proceedings of the Royal Society A, Mathematical, Physical and Engineering Sciences*, Vol. 467, No. 2125, 2011, pp. 144–165. https://doi.org/10.1098/rspa.2010.0172.

[58] Spalart, P. R., and Shur, M. L., "Variants of the Ffowcs Williams - Hawkings Equation and Their Coupling with Simulations of Hot Jets," *International Journal of Aeroacoustics*, Vol. 8, No. 5, 2009, pp. 477–491. https://doi.org/10.1260/147547209788549280.

[59] Mendez, S., Shoeybi, M., Lele, S. K., and Moin, P., "On the Use of the Ffowcs Williams-Hawkings Equation to Predict Far-Field Jet Noise from Large-Eddy Simulations," *International Journal of Aeroacoustics*, Vol. 12, No. 1-2, 2013, pp. 1–20. https://doi.org/10.1260/1475-472X.12.1-2.1.

[60] Welch, P., "The use of fast Fourier transform for the estimation of power spectra: A method based on time averaging over short, modified periodograms," *IEEE Transactions on Audio and Electroacoustics*, Vol. 15, No. 2, 1967, pp. 70–73. https://doi.org/10.1109/TAU.1967.1161901.

[61] Virtanen, P., Gommers, R., Oliphant, T. E., Haberland, M., Reddy, T., Cournapeau, D., Burovski, E., Peterson, P., Weckesser, W., Bright, J., van der Walt, S. J., Brett, M., Wilson, J., Millman, K. J., Mayorov, N., Nelson, A. R. J., Jones, E., Kern, R., Larson, E., Carey, C. J., Polat, İ., Feng, Y., Moore, E. W., VanderPlas, J., Laxalde, D., Perktold, J., Cimrman, R., Henriksen, I., Quintero, E. A., Harris, C. R., Archibald, A. M., Ribeiro, A. H., Pedregosa, F., van Mulbregt, P., and SciPy 1.0 Contributors, "SciPy 1.0: Fundamental Algorithms for Scientific Computing in Python," *Nature Methods*, Vol. 17, 2020, pp. 261–272. https://doi.org/10.1038/s41592-019-0686-2.

[62] Harris, C. R., Millman, K. J., van der Walt, S. J., Gommers, R., Virtanen, P., Cournapeau, D., Wieser, E., Taylor, J., Berg, S., Smith, N. J., Kern, R., Picus, M., Hoyer, S., van Kerkwijk, M. H., Brett, M., Haldane, A., del Río, J. F., Wiebe, M., Peterson, P., Gérard-Marchant, P., Sheppard, K., Reddy, T., Weckesser, W., Abbasi, H., Gohlke, C., and Oliphant, T. E., "Array programming with NumPy," *Nature*, Vol. 585, No. 7825, 2020, pp. 357–362. https://doi.org/10.1038/s41586-020-2649-2.

[63] Israeli, M., and Orszag, S. A., "Approximation of radiation boundary conditions," *Journal of Computational Physics*, Vol. 41, No. 1, 1981, pp. 115–135. https://doi.org/10.1016/0021-9991(81)90082-6.

[64] Colonius, T., "MODELING ARTIFICIAL BOUNDARY CONDITIONS FOR COMPRESSIBLE FLOW," *Annual Review of Fluid Mechanics*, Vol. 36, No. 1, 2004, pp. 315–345. https://doi.org/10.1146/annurev.fluid.36.050802.121930.

[65] Geuzaine, C., and Remacle, J.-F., "Gmsh: A 3-D finite element mesh generator with built-in pre- and post-processing facilities," *International Journal for Numerical Methods in Engineering*, Vol. 79, No. 11, 2009, pp. 1309–1331. https://doi.org/10.1002/nme.2579.

[66] Choi, H., and Moin, P., "Grid-point requirements for large eddy simulation: Chapman's estimates revisited," *Physics of Fluids*, Vol. 24, No. 1, 2012, pp. 011702–1–011702–5. https://doi.org/10.1063/1.3676783.

[67] Jørgensen, F. E., "How to Measure Turbulence with Hot-Wire Anemometers - a Practical Guide," Technical Report, DANTEC Dynamics, Skovlunde, Denmark, 2002.

[68] Guitton, A., "Etude expérimentale des relations entre les champs hydrodynamiques et acoustiques des jets libres," Ph.D. thesis, Faculté des Sciences Fondamentales et Appliquées, Poitiers, France, 2009.